Designing High-Efficiency Thin Silicon Solar Cells Using Parabolic-Pore Photonic Crystals

Sayak Bhattacharya and Sajeev John

Phys. Rev. Applied **9**, 044009 — Published 6 April 2018

DOI: 10.1103/PhysRevApplied.9.044009

Designing high-efficiency thin-silicon solar cells using parabolic-pore photonic crystals

Sayak Bhattacharya and Sajeev John*

Department of Physics, University of Toronto, 60 St. George Street, Toronto M5S 1A7, Ontario, Canada

We demonstrate the efficacy of wave-interference based light-trapping and carrier transport in parabolic-pore photonic crystal, thin-crystalline silicon ($c-Si$) solar cells to achieve above 29% power conversion efficiencies. Using rigorous solution of Maxwell's equations through a standard finite difference time domain (FDTD) scheme, we optimize the design of the vertical-parabolic-pore photonic crystal (PhC) on a 10 μm thick $c-Si$ to obtain a maximum achievable photocurrent density (MAPD) of 40.6 mA/cm^2, beyond the ray optics, Lambertian light-trapping limit. For a slanted-parabolic-pore PhC, that breaks $x-y$ symmetry, improved light-trapping occurs due to better coupling into parallel-to-interface refraction (PIR) modes. We achieve optimum MAPD of 41.6 mA/cm^2 for a tilt angle of 10° with respect to the vertical axis of the pores. This MAPD is further improved to 41.72 mA/cm^2 by introducing a 75 nm SiO_2 anti-reflection coating (ARC) on the top of the solar cell. We use this MAPD and associated charge-carrier generation profile as input for numerical solution of the Poisson's equation coupled with semiconductor drift-diffusion equations using a Shockley-Read-Hall and Auger recombination model. Using experimentally achieved surface recombination velocities of 10 cm/s, we identify semiconductor doping profiles that yield power conversion efficiency over 29%. Practical considerations of additional upper-contact losses suggest efficiencies close to 28%. This improvement beyond the current world record is largely due to an open-circuit voltage approaching 0.8 V enabled by reduced bulk recombination in our thin-silicon architecture while maintaining a high short-circuit current through wave-interference-based light-trapping.

* john@physics.utoronto.ca

I. INTRODUCTION

Crystalline silicon ($c-Si$) offers a reliable platform for high-efficiency solar cells [1] owing to the abundance of high-grade Si and the maturity of fabrication techniques. In the absence of non-radiative recombination and assuming perfect solar absorption, the maximum efficiency of a silicon solar cell at room temperature is given by the Shockley-Queisser (SQ) limit of close to 33% [2]. Recent study by Richter et al. puts an upper bound of 29.4% on the conversion efficiency of a single-junction $c-Si$ cell by taking into account intrinsic recombination loss in the bulk of the semiconductor [3]. Recently, a record power conversion efficiency of 26.3% was obtained by Kaneka Corporation [4, 5] using 165 μm $c-Si$ wafer and a combination of interdigitated back contact (IBC) and heterojunction back contact. This cell exhibits an open circuit voltage (V_{OC}) of 0.744 V. One route to higher V_{OC} and efficiency is to decrease the $Si-$thickness for reduced bulk recombination when the Si surface is well passivated [6–8]. For example, $V_{OC} = 0.760$ V was experimentally achieved by Herasimenka et al. in a 50 μm thick $c-Si$ single heterojunction (SHJ) solar cell [7]. However, thinner Si active layer decreases optical absorption and short circuit current density, J_{SC}, unless a new light-trapping mechanism is used. Photonic crystal (PhC) [9, 10] thin-films offer a novel wave-interference based light-trapping mechanism. Previous studies have shown that texturing the front surface of the solar cell with modulated nano-wires [11], straight and slanted conical nano-pores [12], inverted pyramids [13] helps in coupling the incident sunlight to the photonic crystal over the broad wavelength range of the solar AM1.5 global spectrum without much reflection. Phenomena such as parallel-to-interface refraction (PIR) [14] play a pivotal role in significantly improving light absorption over $800-1100$ nm wavelength range where a thin $c-Si$ active layer would otherwise absorb almost nothing. Optimization studies involving rigorous finite difference time domain (FDTD) solution of Maxwell's equations have shown that wave-interference based light-trapping can surpass the statistical ray-trapping (Lambertian) limit [15] enabling unprecedented values for the maximum achievable photocurrent density (MAPD) [12]. Out of these different PhC architectures, inverted pyramid structure can be mass-fabricated conveniently and accurately via low-cost wet-etching techniques [16, 17]. However, non-optimized designs [17] offer a MAPD of 34.5 mA/cm^2 with a 10 μm thick Si which limits the efficiency to 15.7%. Optimization studies by Eyderman et al. [13] have shown that a 10 μm $c-Si$ inverted pyramid structure yields a MAPD (J_{MAPD}) of 42.5 mA/cm^2. This is only slightly below the MAPD of 43.5 mA/cm^2 corresponding to perfect absorption of the solar AM1.5 spectrum over the wavelength range of $300-1100$ nm. Combining such inverted pyramid thin-films with perovskites to form a tandem solar cell, it is possible to achieve efficiency over 30% [18].

The underlying physics of wave-interference based light-trapping that distinguishes it from the Lambertian ray-trapping picture consists two striking physical phenomena. The realization of these effects over the $700-1100$ nm wavelength band requires the fabrication of photonic crystals with specific architectures and wavelength-scale periodicity. The first of these two effects is the deflection of sunlight into directions nearly parallel to the air-silicon boundary, rather than the Lambertian $\cos\theta$ distribution where θ is the angle of deflection relative to the normal. This parallel-to-interface refraction [14], leads to considerably longer path length augmentation within silicon than the $4n^2$

Lambertian enhancement (where n is the refractive index of the material). This is a wave-interference effect beyond the scope of ray-optics. The second physical effect is the slow group velocity of electromagnetic modes in the higher bands of the PhC band structure. Sunlight captured into these slow light modes exhibit a very long dwell time in the material, over and above that suggested by the physical path length enhancement due to the first effect. These two effects combined enable thin films ($3-10$ μm thick) of silicon to absorb sunlight far beyond the Lambertian limit in the $700-1100$ nm range and somewhat beyond the Lambertian limit when integration is considered over the entire $300-1100$ nm wavelength range. While the PhC solar cell architectures we describe in this paper have thickness considerably beyond the actual PhC depth, these wave-interference effects are clearly seen in a high density of optical resonances (and their electromagnetic field profiles) over the long wavelength range of the absorption spectrum.

Another architecture exhibiting wave-interference based solar light-trapping for thin $c-Si$ solar cells is the parabolic pore photonic crystal. Unlike the inverted pyramid structure, this structure is fabricated using reactive ion etching (RIE) [19]. It was shown earlier [19] that this 10 μm thick teepee-like PhC with a lattice constant of 1200 nm exhibits $J_{MAPD} = 39.1$ mA/cm^2, slightly below the Lambertian light-trapping limit (Lambertian absorption yields 39.65 mA/cm^2 for the wavelength range of $300-1100$ nm). For a lattice constant of 850 nm $J_{MAPD} = 39.7$ mA/cm^2, slightly above the Lambertian limit.

Our approach to improving solar cell efficiency remains within the bounds of Shockley-Queisser limit. However by surpassing the Lambertian limit for solar absorption and reducing bulk non-radiative Auger recombination through the use of a thin-silicon photonic crystal, the so-called practical efficiency limit of 29.4% no longer applies to our designs. A variety of other proposals have been made to surpass the Shockley-Queisser limit itself by absorbing sunlight below the electronic bandgap of silicon. This involves intermediate band architectures [22, 23] or non-linear optical upconversion architectures [24]. These approaches increase MAPD beyond 43.5 mA/cm^2 but involve more complex architectures and typically introduce further issues of non-radiative recombination loss. In the present manuscript, we identify an important and practical way to improve solar cell efficiency within Shockley-Queisser bound before looking beyond it.

In this article, we describe how pore optimization and symmetry-breaking improve the MAPD toward the perfect absorption limit of 43.5 mA/cm^2 without increasing the $c-Si$ active layer thickness. This enables high J_{SC} and V_{OC} exceeding 0.75 V, allowing thin-film silicon solar cells to surpass 29% efficiency. For inverted pyramids fabricated by wet-etching, for a given lattice constant (a), the height of the pyramids (h) is fixed by the etching angle $\alpha = 54.7^{\circ}$ between (111) and (100) planes of $c-Si$ wafer. In contrast, parabolic pore structures made by RIE, allow variation of (h/a). The factor (h/a) is an important optimization parameter for light-trapping in parabolic pore PhC solar cells. Specifically, an increasing (h/a) results in a more gradual refractive index variation between air and Si which improves the anti-reflection of the parabolic pore PhC. However, this decreases light absorbing material from the solar cell leading to an optimal (h/a) factor. Our optimization study shows that for $a = 1000$ nm and $(h/a) = 1.7$, we obtain the best $J_{MAPD} = 40.57$ mA/cm^2 for a symmetric parabolic pore structure. This MAPD exceeds the Lambertian limit as well as $J_{MAPD} = 39.7$ mA/cm^2 reported earlier [19]. A significant improvement occurs by breaking the $x-y$

symmetry of the structure by tilting the parabolic pores. The tilted parabolic pore PhC provides better light-trapping, yielding $J_{MAPD} = 41.6$ mA/cm^2 without anti-reflection coating (ARC) and $J_{MAPD} = 41.72$ mA/cm^2 with 75 nm SiO_2 ARC. Our numerical investigation reveals that slanted parabolic pore couples more energy into PIR modes in the $900 - 1000$ nm wavelength range than their vertical counterparts. In general, Lambertian limit is valid for any angle of incidence of the incoming sunlight. At normal incidence, our optimized slanted parabolic-pore PhC exceeds the Lambertian limit by ~ 2 mA/cm^2. Consequently, our optimized cell would exhibit beyond-Lambertian limit light-trapping within a cone of angle 2α, where α is the angle of incidence of the incoming sunlight at which the MAPD of the cell drops by 2 mA/cm^2 as compared to the MAPD at normal incidence.

In general, it is time consuming to perform a high-resolution, $3D$ drift-diffusion calculation for a 10 μm thick solar cell. For simplicity, we carry out transport calculations for an effective one dimensional model using an algorithm (described in sec. II) that uses a spatially averaged generation profile and MAPD of the $3D$ FDTD calculation as input to the equivalent one dimensional solar cell. We benchmark our $1D$ calculation against the 25% efficient passivated emitter and rear locally diffused (PERL) cell [20, 21, 25] and verify good agreement between our $1D$ calculation and experimentally obtained PERL cell current-voltage characteristics. Our numerical results show that it is possible to obtain beyond 29% efficiency with 10 μm thick solar cell textured by slanted parabolic pores when the effective surface recombination velocities (SRVs) of the front and rear contacts approach 10 cm/s. Although such low values of SRV have been achieved experimentally for a planar Si wafer with low doping [26], it is challenging to achieve such low SRVs for $c-Si$ with high emitter doping [27]. The 25% efficient PERL cell [25] has relatively lower emitter doping than that considered in [27] and consequently, lower front surface recombination velocities for electrons (S_n) and holes (S_p). Recent study has shown that S_n, S_p and trapped charge density of the 25% efficient PERL cell yield an effective front surface recombination velocity (SRV_{front}) of 100 cm/s for a donor doping of 10^{18} cm^{-3} [28]. We consider the influence of higher front SRV on our cell-performance in sec. V. We also optimize the emitter thickness and doping profile taking into account the power-loss in emitter region due to sheet resistance. Our simulations show that inclusion of such real-world effects allows our 10 μm thick $c-Si$ cell to reach a conversion efficiency of 28%, still well beyond the current world record.

In this paper, we do not include detailed consideration of optical shadowing effects of the upper electrical contacts. Roughly speaking, any percentage loss of solar absorption in silicon due to shadowing will lead to a corresponding (multiplicative) percentage loss in efficiency. Experimental measurements in [29] have shown that a front-contact geometry with 20 μm finger-width and 800 μm finger-spacing leads to $\sim 1\%$ shading loss of J_{SC}. For our proposed cell with the same contact geometry, this corresponds to $\sim 0.3\%$ (additive) loss of efficiency. However, two recent approaches can be used to recover major part of this small loss. The first is the use of interdigitated back contact (IBC) cells [30–32]. Accurate simulation of an IBC cell would require at least a $2D$ transport model for photo-generated charge carriers [33]. The second approach is the application of a dielectric coating over the contacts that effectively "cloaks" them by refracting nearly all incident sunlight "around" the metal fingers [34–37].

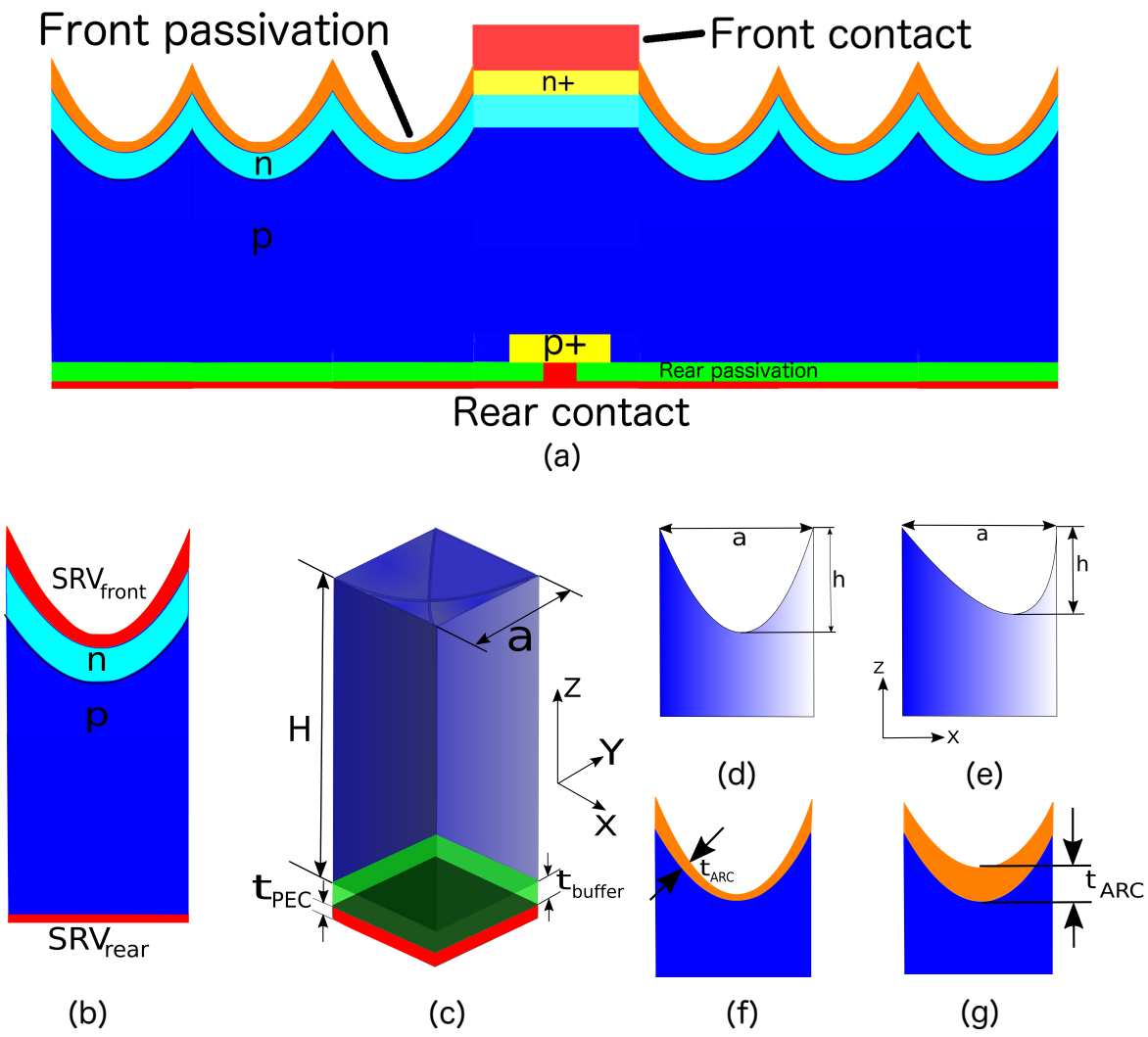

Figure 1. Parabolic pore PhC solar cell architecture: (a) cross-sectional view of the $3D$ cell (not to scale). (b) model used for carrier transport calculations. The details of the contact and passivation geometries, effect of passivation, BSF etc. are accounted for by SRV_{front} and SRV_{rear}. (c) unit cell of the parabolic pore PhC. The buffer layer and the PEC back-reflector are shown by green and red slabs, respectively. (d) and (e) show the $xz-$ view of the vertical and slanted parabolic pores, respectively. The $yz-$view of both architectures are same as (d). (f) and (g) show the conformal and non-conformal ARC layers, respectively.

II. SOLAR CELL ARCHITECTURE AND COMPUTATION DETAILS

We consider two light-trapping geometries: vertical and slanted parabolic pore PhCs, depicted in fig. $1(c)-(g)$. The PhCs are periodic in the $xy-$plane with a lattice constant a along both x and $y-$directions. The active layer of the solar cell is a $c-Si$ slab of thickness H, backed by a perfect electric conductor (PEC) mirror that prevents light from escaping the solar cell through the rear surface. The PEC layer has a thickness, $t_{PEC} = 100$ nm. A SiO_2 buffer layer, with thickness t_{buffer} and refractive index n_{buffer}, placed between the back-reflector and $c-Si$ slab acts as rear passivation. As we describe in sec. III, a glass buffer layer with $t_{buffer} = 75$ nm also provides a slight enhancement in light-trapping. The vertical parabolic pores at the front surface of the $c-Si$ slab have a depth h

(shown in fig. $1d$).

A cross-sectional view of the PhC based solar cell is shown in fig. $1(a)$. The emitter of the solar cell is a very thin conformal (width $t_{emitter} = 100$ nm) $n-$type region with a doping density N_d and the base region is $p-$type with a doping density N_a. The PEC at the rear surface of the cell makes contact with the active layer through highly $p-$doped (p^+) back surface field (BSF) regions and serves as the rear contact to the solar cell. Similarly, an insulating layer of SiO_x or SiN_x [38, 39] at the front surface of the cell acts as front passivation. The shape of the passivation layer influences the optical performance of the cell since, it also acts as ARC for incoming sunlight. We consider both conformal (fig. $1f$) and non-conformal (fig. $1g$) models of the front ARC layer in our optical calculations. In case of conformal geometry, t_{ARC} denotes the thickness normal to the parabolic shape whereas in the non-conformal case t_{ARC} denotes the vertical height of the ARC. The front electrodes can be made of either indium tin oxide (ITO) or metal which make contact to the PhC through highly $n-$doped (n^+) regions. In order to provide a concrete model of sheet-resistance, the spacing between the front-contact fingers can be assumed to be roughly 800 μm with 20 μm finger-width. This configuration is same as that used in 25% efficient PERL cell [20].

In order to break the $x-y$ symmetry, the vertical parabola is rotated anti-clockwise by an angle θ about the $y-$axis. In the rotated coordinate system defined by $x' = x\cos\theta - z\sin\theta$ and $z' = x\sin\theta + z\cos\theta$, the slanted parabola is defined by $z' = kx'^2$, where k is determined from (h/a) of the pores. The solution of this quadratic equation defines the slanted parabolic profile in the original coordinate system.

$\theta = 0^\circ$ corresponds to the vertical parabolic pore case. In our FDTD calculation, we vary θ over a range of $0 - 15^\circ$ to study the effect of $x - y$ symmetry breaking on the light trapping capability of PhC. The cross-sectional view of the slanted parabolic pore is shown in fig. $1(e)$.

Our $3D$ FDTD calculations were performed using the open source Electromagnetic Template Library (EMTL) [40]. Periodic boundary condition is applied along x and $y-$ directions and perfectly matched layers (PML) are placed at the computation boundaries normal to $z-$direction. The solar cell is illuminated by a normally incident broadband plane wave that contains significant energy in the wavelength range of $300 - 1100$ nm. The reflection (R) and transmission (T) are measured by placing two flux planes: one between the cell and the computation box boundary at the top and the other one between the PEC and the computation box boundary at the bottom. Since there is no absorption in PEC, the total absorption $A(\lambda)$ in the active layer of the solar cell is given by $A(\lambda) = 1 - R(\lambda) - T(\lambda)$.

The number of photons absorbed by the solar cell at a given wavelength λ can be found by multiplying the number of incident photons with $A(\lambda)$. The total number of incident photons at a wavelength λ is given by $\lambda I(\lambda)/hc$, where $I(\lambda)$ is the intensity of the incident AM 1.5 global spectrum, h is Planck's constant and c is the speed of light in vacuum. We assume that each of these absorbed photon produces one electron-hole pair. MAPD represents the short circuit current produced by the solar cell when all the generated carriers are collected at the electrodes without any loss. Thus, the MAPD generated over a wavelength range of $300 - 1100$ nm is given by:

$$J_{MAPD} = \int_{\lambda=300\text{ nm}}^{\lambda=1100\text{ nm}} \frac{e\lambda}{hc} I(\lambda) A(\lambda) d\lambda \tag{1}$$

In order to evaluate the electronic performance of our proposed solar cell, carrier drift-diffusion equations are numerically solved using the open source software package Microvolt [41]. To avoid a time-consuming $3D$ transport calculation, we use an equivalent $1D$ model in Microvolt that accurately recaptures the $J-V$ characteristic of the actual $3D$ solar cell. The thickness of the $c-Si$ in the $1D$ model is kept same as that of the $3D$ cell. The detailed geometries of the contacts, passivation layers and BSF are subsumed into effective values for the surface recombination velocities of the front and rear contacts of the equivalent $1D$ cell. These SRVs enter the computation as boundary conditions for the drift-diffusion equations. A $1D$ generation profile can be obtained by integrating the actual $3D$ generation profile obtained by EMTL in the $x-$ and $y-$directions within a unit. We find, however, that the precise details of the generation profile have a nearly negligible influence on the resulting $J-V$ characteristics. Accordingly, we used a simplified $1D$ generation profile that imparts different Beer-Lambert absorption profiles for each wavelength according to the wavelength dependent decay constants $\alpha(\lambda) = 4\pi k(\lambda)/\lambda$, where $k(\lambda)$ is the imaginary part of the refractive index of $c-Si$ [42].

The equivalent $1D$ generation profile for our $3D$ solar cell is determined by a two step procedure. First, we set the diffusion length very large compared to the cell thickness and set the front and rear SRVs very small (in order to ensure negligible recombination both in the bulk and at the surface). We define the short circuit current produced by the $1D$ cell (in absence of any recombination loss) as J_{SC0}. We then scale up the overall generation profile such that $J_{SC0} \rightarrow J_{MAPD}$ of our $3D$ solar cell.

In order to verify the accuracy of our algorithm we use our $1D$ transport calculation to reproduce the V_{OC}, J_{SC}, conversion efficiency (η) and fill factor (FF) of the 25% efficient PERL cell [20, 21, 25]. The doping dependent mobilities of the electrons and holes are implemented using the model of Masetti et al. [43]. In our computation, we consider two different models of bulk recombination. It has been shown that hydrogenation of Czocharlski grown $c-Si$ wafers can increase bulk minority carrier lifetimes substantially by passivating the bulk defect states [44]. Further experimental studies in [45–47] have shown that it is possible to achieve lifetimes exceeding the intrinsic Auger limit. Consequently in the first model we choose the diffusion lengths, L_n and L_p, of the electrons and holes somewhat independently of the doping concentrations. For a particular doping level, the mobility of the carriers is set by the Masetti et al. model [43] and the diffusivities, D_n and D_p, of the electrons and holes are calculated from Einstein's relation. For a given L_n (or L_p) the effective bulk lifetime τ_{neff} (or τ_{peff}) is given by $\tau_{neff} = L_n^2/D_n$.

In the second model, we take into account Auger recombination which fixes the diffusion length for a given doping. In this case, we calculate Auger lifetime (τ_{Aug}) using the model of Kerr and Cuevas [48]. The Shockley-Read-Hall (SRH) recombination is accounted for by assuming the SRH lifetime, $\tau_{SRH} = 1.2$ ms. We then calculate the effective bulk lifetime τ_{eff} from the following relation:

$$\frac{1}{\tau_{eff}} = \frac{1}{\tau_{SRH}} + \frac{1}{\tau_{Aug}} \tag{2}$$

Using these input parameters, the semiconductor drift-diffusion equations are numerically solved for various doping levels, diffusion lengths/bulk lifetimes and effective front/rear SRVs to obtain the $J-V$ characteristics of the solar cell. From the $J-V$ characteristics we obtain J_{SC}, V_{OC}, the fill factor (FF) and the power conversion efficiency:

$$\eta = FF\frac{J_{SC}V_{OC}}{P_{inc}} \tag{3}$$

Here, $P_{inc} = 1000$ w/m^2, is the incident power of the AM 1.5 global spectrum.

III. LIGHT TRAPPING OPTIMIZATION

Wave-interference based light-trapping plays an essential role in enabling a next-generation thin-film silicon solar cell to absorb as much as its conventional counterparts $10-50$ times thicker. PhC-based optical resonances provide an effective way to increase the lifetime of near-infrared photons in the active layer. We now present the results of our light-trapping optimization studies for both vertical and slanted parabolic-pore PhCs. In case of the vertical parabolic-pore PhC, we vary the height (h) of the pores for different values of a. In a RIE setup this can be achieved by varying the etching power. The parabolic-pore PhC combines the advantages of parallel-to-interface refraction and light-trapping multiple coherent scattering events in the $x-y$ plane and suppressed reflection enabled by the gradual profile variation in the $z-$direction. As we increase (h/a), the parabolic pore presents a more gradual anti-reflective profile but as more Si is etched away, the photo-generation volume is decreased. These two competing effects define an optimum (h/a) for a given a.

Figure 2(a) shows the MAPD optimization map for vertical parabolic pore PhC solar cell with $H = 10$ μm, $t_{buffer} =$ 75 nm and $n_{buffer} = 1.5$. An optimum MAPD of 40.57 mA/cm^2 is achieved for $a = 1000$ nm and $(h/a) = 1.7$. There are few more hotspots in the optimization map which offer MAPDs beyond 40 mA/cm^2: $a = 1300$ nm, $(h/a) = 1.8$ with MAPD= 40.1 mA/cm^2; $a = 1800$ nm, $(h/a) = 2.1$ with MAPD= 40.45 mA/cm^2; $a = 1700$ nm, $(h/a) = 2.2$ with MAPD 40.51 mA/cm^2 and $a = 1200$ nm, $(h/a) = 2.5$ with MAPD 40.53 mA/cm^2. The last 3 hotspots among these offer MAPD which is very close to our optimum point. However, shallower pores are easier to etch and lead to a more robust structure, so we focus attention on $a = 1000$ nm, $(h/a) = 1.7$. We note that the optimum (h/a) shifts higher for larger lattice constants. The corresponding optimization map for $a > 2000$ nm is shown in fig. 2(b). For $a = 2200$ nm and $(h/a) = 2.1$, we find a weaker local maxima with MAPD= 39.9 mA/cm^2. Clearly, the optimization of parabolic-pore PhC is different from that of the inverted-pyramid PhC [13]. The 10 μm thick inverted-pyramid PhC solar cell has its optimum MAPD for $a = 2500$ nm whereas the 10 μm thick parabolic-pore PhC solar cell has

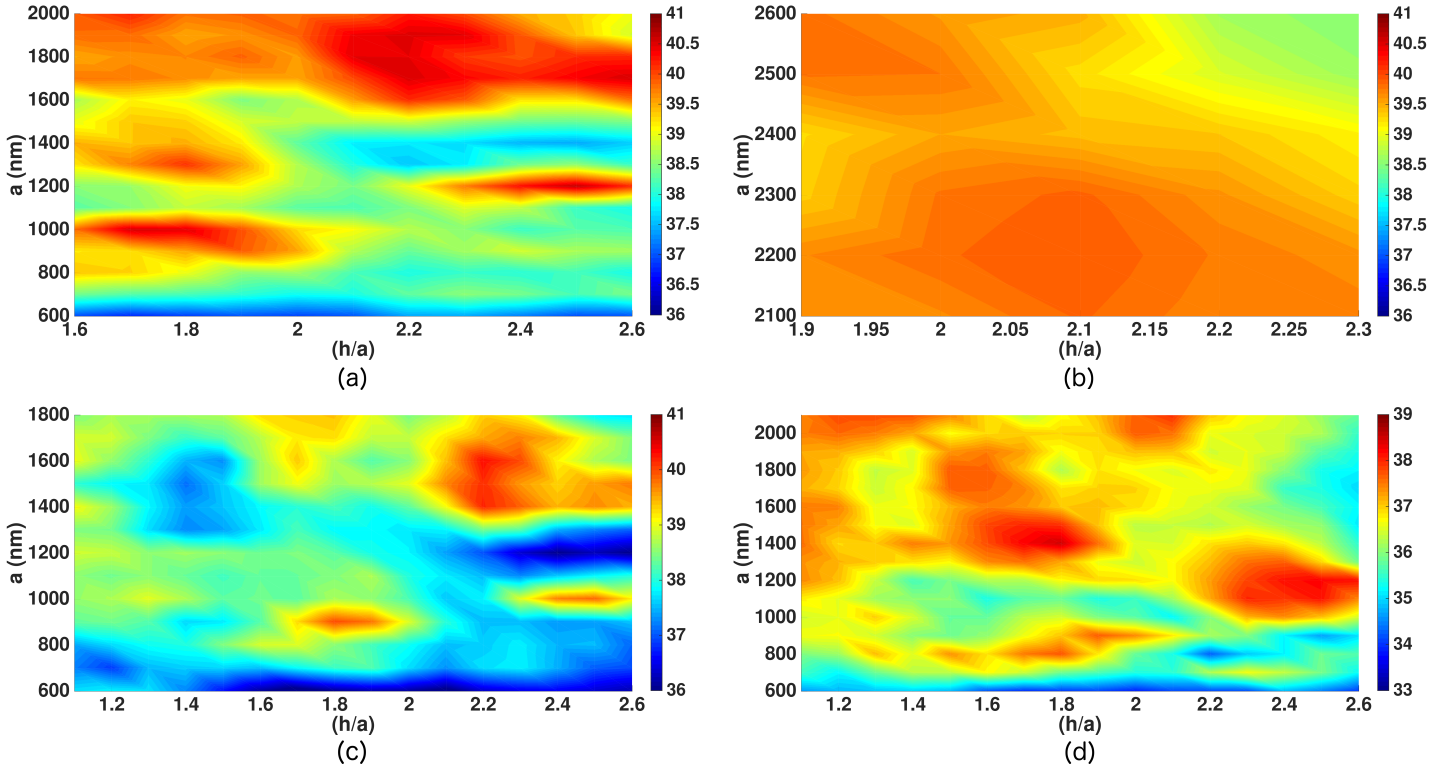

Figure 2. Optimization map for MAPD in vertical parabolic pore PhC: (a) and (b) $H = 10$ μm, (c) $H = 8$ μm and (d) $H = 5$ μm. For each of these cases $t_{PEC} = 100$ nm, $t_{buffer} = 75$ nm and $t_{ARC} = 0$. For $H = 10$ μm, optimum MAPD of 40.57 mA/cm^2 is obtained for $a = 1000$ nm and $(h/a) = 1.8$. For $H = 8$ μm, optimum MAPD value is 40.29 mA/cm^2 for $a = 1800$ nm and $(h/a) = 2.2$. However, obtaining $(h/a) = 2.2$ can be difficult from fabrication point of view. So, $a = 900$ nm, $(h/a) = 1.8$ with MAPD 39.98 mA/cm^2 can be chosen as optimum point in (c). For $H = 5$ μm, the optimum point is $a = 1400$ nm, $(h/a) = 1.8$ with MAPD 38.48 mA/cm^2.

its best solar absorption for $a = 1000$ nm.

Figure 2(c) and (d) show the optimization maps for thinner silicon films of $H = 8$ μm and $H = 5$ μm, respectively. For $H = 8$ μm, we find 3 local maxima offering substantial MAPD: $a = 1600$ nm, $(h/a) = 2.2$ with MAPD 40.29 mA/cm^2; $a = 1000$ nm, $(h/a) = 2.5$ with MAPD 39.83 mA/cm^2 and $a = 900$ nm, $(h/a) = 1.8$ with MAPD 39.98 mA/cm^2. For $H = 5$ μm the hotspots are located at: $a = 1400$ nm, $(h/a) = 1.8$ with MAPD 38.48 mA/cm^2; $a = 1200$ nm, $(h/a) = 2.5$ with MAPD 38.2 mA/cm^2 and $a = 800$ nm, $(h/a) = 1.8$ with MAPD 37.71 mA/cm^2. Out of the hotspots in the optimization maps of fig. 2, one particular extremum exhibits interesting characteristics. If we scan through the optimization maps keeping (h/a) fixed at 1.8, we see that there is always a maxima near $a = 800 - 1000$ nm irrespective of H. These peaks corresponding to $(h/a) = 1.8$ have been shown in fig. 3. As H is decreased the peak shifts towards lower a. Thus, the factor $(h/a) = 1.8$ is a robust ratio with respect to thickness variation of the solar cell. Also, a comparison of the hotspots in the optimization maps suggests that the maxima corresponding to this ratio is narrower with respect to variation of lattice constant as compared to other hotspots which appear to be broader. Broader maxima suggest considerable robustness to disorder effects.

While the buffer layer provides rear passivation to the solar cell, it can also improve light trapping (see Fig. 4). In

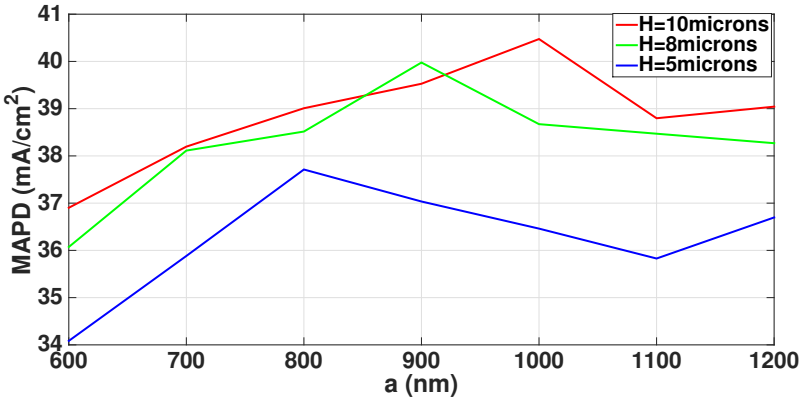

Figure 3. Existence of a robust ratio $(h/a) = 1.8$: this ratio exhibits local maxima in the optimization map in the range $800 \leq a \leq 1000$ nm for $H = 5, 8$ and 10 μm. As we decrease the active layer thickness, the peak shifts from a higher lattice constant to a lower lattice constant.

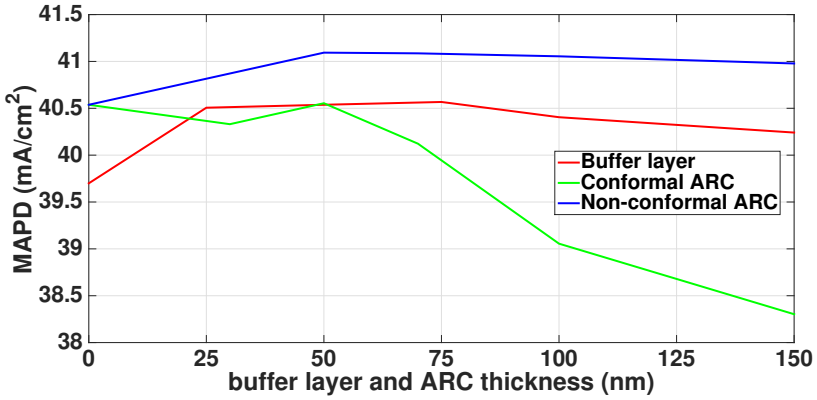

Figure 4. Optimization of buffer layer thickness (t_{buffer}) and ARC thickness (t_{ARC}). Optimized values of t_{buffer} and t_{ARC} (non-conformal) are 75 nm and 50 nm, respectively. Also, non-conformal ARC performs better than the conformal geometry.

absence of the buffer layer the MAPD of the solar cell is only 39.7 mA/cm^2 for $a = 1000$ nm and $h = 1700$ nm. By introducing a 25 nm thick buffer of glass ($n_{buffer} = 1.5$), the MAPD improves by 0.8 mA/cm^2 to 40.51 mA/cm^2. The optimum value of t_{buffer} is 75 nm providing the previously quoted MAPD of 40.57 mA/cm^2. Further, we investigate the effect of front passivation layer or the ARC on the optical performance of the solar cell. Figure 4 suggests that a non-conformal ARC layer is better than a conformal ARC as the former improves the MAPD by 0.52 mA/cm^2 for an optimum thickness of 50 nm whereas the conformal ARC does not improve the MAPD. Overall, for $a = 1000$ nm, $h = 1700$ nm, $t_{buffer} = 75$ nm and a non-conformal ARC of thickness 50 nm, we obtain the optimum MAPD of 41.09 mA/cm^2 for the 10μm thick solar cell textured with vertical parabolic pore PhC.

An improvement to the MAPD is realized if we break the $x-y$ symmetry of the structure by tilting the pores along the $x-$direction according to the method outlined in sec. II. We keep the lattice constant fixed at 1000 nm, (h/a) at 1.7 and the tilt angle θ is varied over a range of $0 - 15°$. We excite the structure separately with $x-$polarized and $y-$polarized plane waves in order to study the polarization response of the structure. The MAPD values corresponding to different tilt angles are shown in fig. 5 for both polarizations. Without any ARC layer, we obtain the optimum

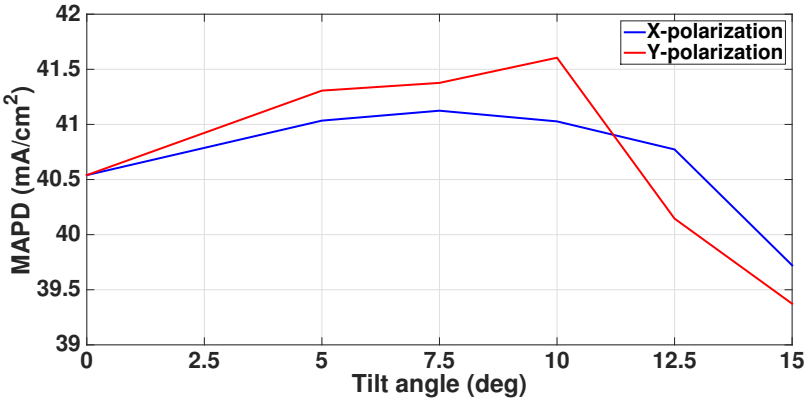

Figure 5. Variation of MAPD of slanted parabolic pore with tilt angle θ for excitations polarized along $x$and y directions. The improvement for $y-$polarized light is more when the pores are tilted along x (shown in fig. $1(e)$.

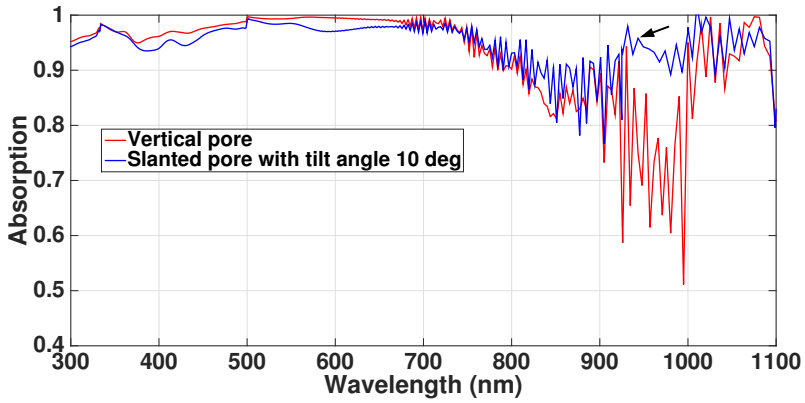

Figure 6. Comparison of absorption spectra under $y-$polarized excitation for $x-y$ symmetric (vertical parabolic pore) structure and $x-y$ symmetry-breaking (slanted parabolic pore) structures. For both cases, $t_{buffer} = 75$ nm, $t_{ARC} = 0$ and $t_{PEC} = 100$ nm. The symmetry-breaking PhC absorbs more light in $750-1010$ nm wavelength range.

MAPD of 41.6 mA/cm^2 for the $y-$polarized case at $\theta = 10°$ which shows an improvement of ~ 1 mA/cm^2 from the $x-y$ symmetric case. For $x-$polarized incident wave the optimum MAPD is 41.1 mA/cm^2 at $\theta = 7.5°$, an improvement of ~ 0.5 mA/cm^2 from the symmetric case. For $\theta = 10°$, the MAPD corresponding to $x-$polarized incident radiation is 41.05 mA/cm^2 and for $\theta = 7.5°$ the MAPD corresponding to $y-$polarized excitation is 41.35 mA/cm^2. Thus, on average we find slightly higher overall MAPD for $\theta = 10°$ than for $\theta = 7.5°$ case.

To understand the underlying cause of the significant MAPD improvement for $y-$polarized light, we compare the absorption spectra of the vertical and slanted parabolic pores in fig. 6. Clearly, the slanted pore absorbs more sunlight in the $750-1010$ nm wavelength range. The arrow in fig. 6 points to 95.6% absorption peak at $\lambda = 940$ nm for the slanted parabolic PhC compared to only 77.2% for its vertical counterpart. In fig. 7, we plot the energy density distributions and in-plane components of the Poynting vectors along orthogonal slices for $y-$polarized excitation. The energy densities are normalized by the incident energy density. Figure $7(a)$ and (b) correspond to the $xz-$plane data slices and fig. $7(c)$ and (d) correspond to yz slices for the vertical and slanted pore PhCs, respectively. Figure $7(a)$ shows a small amount of energy flow parallel to the interface and some vortex-like paths near the intensity peaks.

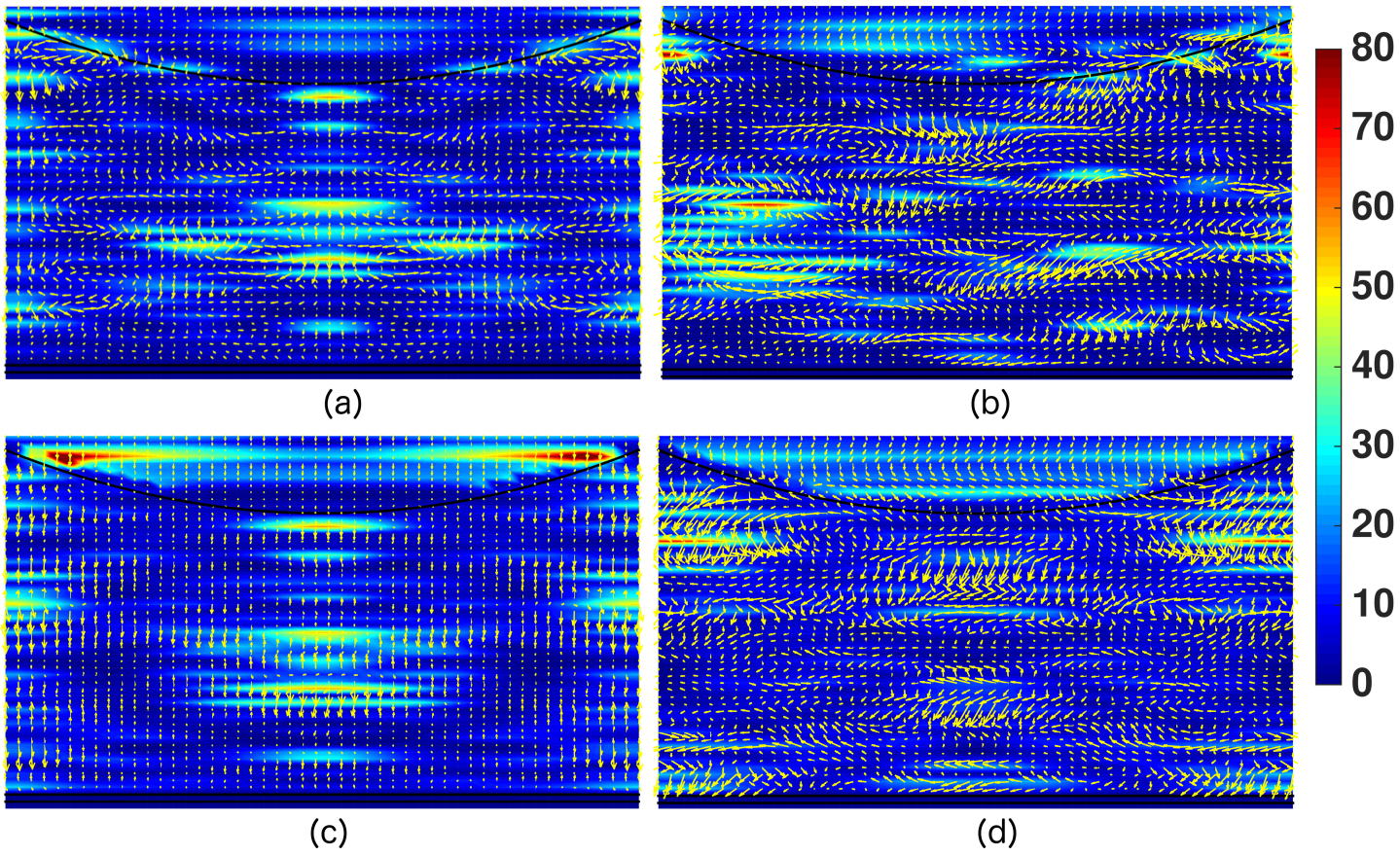

Figure 7. Plot of energy density and in-plane Poynting vector for vertical and slanted pore PhCs at $\lambda = 940$ nm. The incident plane wave is polarized along $y-$direction. (a) and (b) corresponds to the $xz-$slice (passing through the center of the unit cell) for vertical and slanted pores, respectively. The Poynting vectors show significant parallel-to-interface power flow and prominent formation of vortices in (b) as compared to (a). (c) and (d) show the central $yz-$slice for the vertical and slanted pores, respectively. For the vertical pores almost all the power flows from top to bottom. However, (d) shows prominent vortices in the power flow pattern and parallel-to-interface Poynting vectors. Clearly, PIR into slow-light modes is a key mechanism for better light-trapping in the $x - y$ symmetry-broken structure.

In fig. $7(b)$, both parallel-to-interface energy flow and vorticity near the hotspots are significantly more prominent. The same conclusion applies to the $yz-$plane energy flows shown in fig. $7(c)$ and (d). In case of the $x - y$ symmetric PhC the energy flows predominantly along $z-$direction but when we break the $x - y$ symmetry, the Poynting vector exhibits considerable parallel-to-interface energy flow. The resulting long dwell time of photons within the active layer ensures strong absorption.

IV. CARRIER TRANSPORT AND SOLAR CELL PERFORMANCE

We begin by benchmarking our approximate $1D$ transport model against the well-known 25% efficient PERL cell [20, 21, 25]. This cell employs a passivation layer between the back-reflector and active layer. The rear metal contacts the active layer only through highly doped $p-$regions that provide BSF. A similar strategy applies to the front contacts. The overall effect of surface passivation (both chemical and trapped charge) in the $3D$ PERL cell is

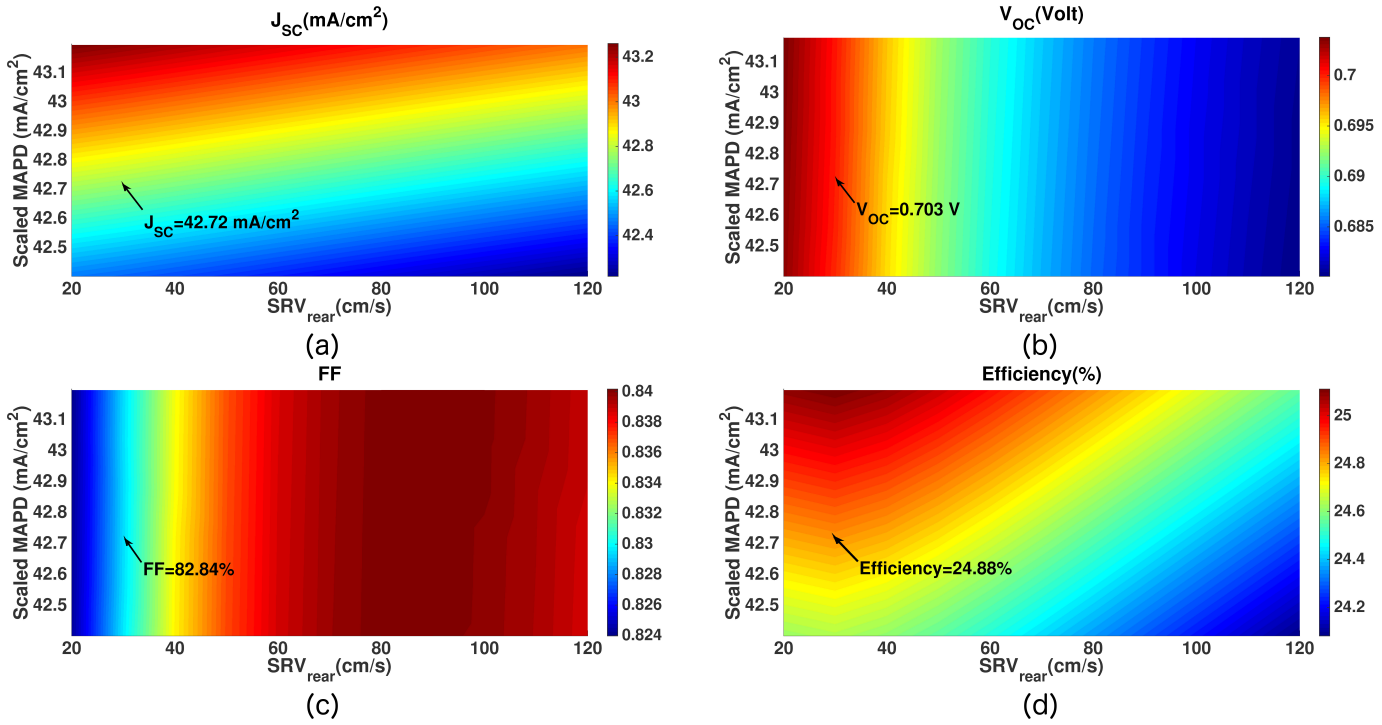

Figure 8. Validation of $1D$ transport model against 25% efficient PERL cell performance parameters. The scaled MAPD for the generation profile (described in sec. II) and SRV_{rear} are treated as independent variables. (a), (b), (c) and (d) correspond to the colormaps of J_{SC}, V_{OC}, FF and η, respectively. The $1D$ model can accurately capture all the experimentally measured PERL cell performance parameters for a unique choice of scaled MAPD= 42.76 mA/cm^2 and $SRV_{rear} = 30$ cm/s.

accounted in our $1D$ model by effective SRVs at the top and bottom of the solar cell. Robinson et al. numerically investigate a $2D$ model of the PERL cell [25]. They consider bandgap-narrowing effect that increases the MAPD of the cell and perimeter recombination [50] that involve adjustment of V_{OC} by 6 mV above the measured value. In our $1D$ model, these effects are not considered, instead the SRVs are chosen to best fit the performance parameters (J_{SC}, V_{OC}, FF and η) of the PERL cell. We model the 400 μm thick PERL cell using an equivalent $1D$ cell of the same thickness with a Gaussian doping profile for the 1 μm thick $n-$type emitter (same as the experimentally measured profile [25]). The Gaussian doping profile for the emitter has a peak value of $5 \times 10^{18} cm^{-3}$ and drops to 1.41×10^{16} cm^{-3} at the junction. The thick $p-$type base region is modeled as a 399 μm thick uniformly doped region with $N_a = 1.41 \times 10^{16}$ cm^{-3}. For carrier recombination, we set $\tau_{SRH} = 1$ ms [25]. The Auger lifetime and effective bulk lifetime of the carriers are modeled according to Eq. 2.

The PERL cell exhibits $J_{SC} = 42.7$ mA/cm^2 suggesting that bandgap narrowing effects expand the solar absorption spectrum to wavelengths slightly larger than 1100 nm. In principle, it is possible to estimate the extent of BGN from knowledge of the detailed doping profile of the PERL cell. However, our aim is to show that our $1D$ model can accurately capture the experimental performance parameters of an actual $3D$ cell through boundary conditions imposed by an effective SRV_{front} and SRV_{rear} that subsumes the effect of BGN. We recapture the experimental J_{SC} (which already involves BGN) of the PERL cell through the scaling parameter discussed in sec. II. The other

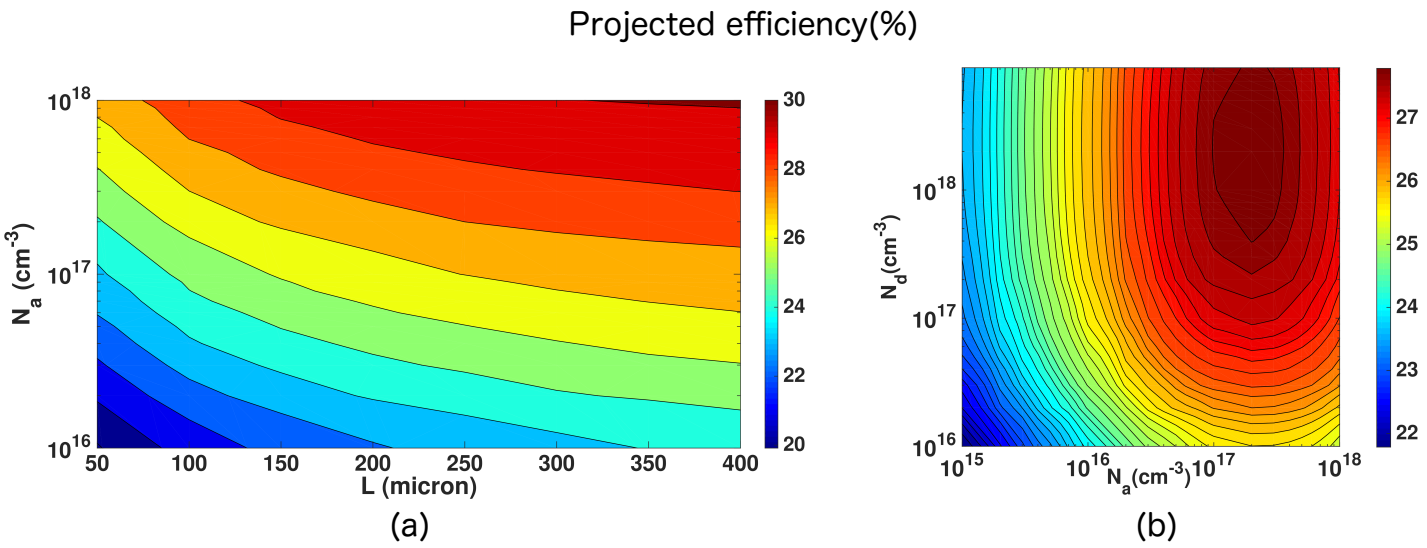

Figure 9. Contour plots of efficiency for: (a) doping-independent diffusion length and (b) doping-dependent lifetime and diffusion length due to Auger recombination. The $pn-$junction is assumed to be located 100 nm below the top passivation-Si interface. For (a), N_d is kept fixed at 10^{18} cm^{-3}. Near 30% efficiency is obtained for $N_a = 1\times10^{18}$ and $L = 300$ μm. (b) shows that Auger recombination reduces the optimum efficiency to 27.94%, achieved for $N_d = 2\times10^{18}cm^{-3}$ and $N_a = 2\times10^{17}cm^{-3}$. In both cases we set $SRV_{front} = SRV_{rear} = 10$ cm/s.

physical manifestation of BGN is slight drop in V_{OC} of the cell. An increase in SRV recaptures this drop in V_{OC}, while maintaining J_{SC} at a constant value (fig.10). In this way, our equivalent SRV_{front} and SRV_{rear} simulates the effect of BGN. Accordingly, in our $1D$ model, we rescale the MAPD along with SRV_{front} and SRV_{rear} in order to recapture the observed characteristics of the PERL cell. Variation in SRV_{front} over the range of $1-200$ cm/s has little effect on the cell performance and so we set $SRV_{front} = 140$ cm/s and vary the MAPD scale factor and SRV_{rear} to recapture the PERL cell performance parameters. The results for J_{SC}, V_{OC}, FF and η are shown in fig. 8. The plots reveal a unique choice of scale factor and SRV_{rear} for which we can reproduce the experimentally obtained $J-V$ characteristics. For MAPD= 42.76 mA/cm^2 and $SRV_{rear} = 30$ cm/s, we obtain $J_{SC} = 42.72$ mA/cm^2, $V_{OC} = 0.703V$, $FF = 82.84\%$ and $\eta = 24.88\%$ as compared to the experimentally measured values of 42.7 mA/cm^2, 0.706 V, $FF = 82.8\%$ and $\eta = 24.96\%$. This suggests a unique mapping of reasonable accuracy between real $3D$ solar cells and our $1D$ transport model, given appropriate choices of MAPD, SRVs and τ_{eff}.

We now consider our best 10 μm thick slanted-pore solar cell exhibiting MAPD of 41.72 mA/cm^2. In our transport calculations we consider a 100 nm thick uniformly doped $n-$type emitter region with $N_d = 1\times10^{18}$ cm^{-3}. Before considering the important Auger recombination model, we vary the carrier diffusion lengths independently of doping and set $L_n = L_p \equiv L$. Both SRV_{front} and SRV_{rear} are fixed to 10 cm/s. Figure 9(a) shows the contour plot of the efficiency when the base doping N_a and diffusion length L are varied. For $N_a = 1\times10^{18}$ and $L = 300$ μm (equivalently, $\tau_{neff} = 0.13$ ms and $\tau_{peff} = 0.22$ ms), the conversion efficiency η reaches $\sim 30\%$. When Auger recombination is included, the optimum efficiency drops to about 28% (Fig. 9b).

In fig. 9(b) we consider the Auger limited model where we vary the doping of the emitter and base to find the optimized doping level. In this model, increased doping leads to more Auger recombination and shorter diffusion

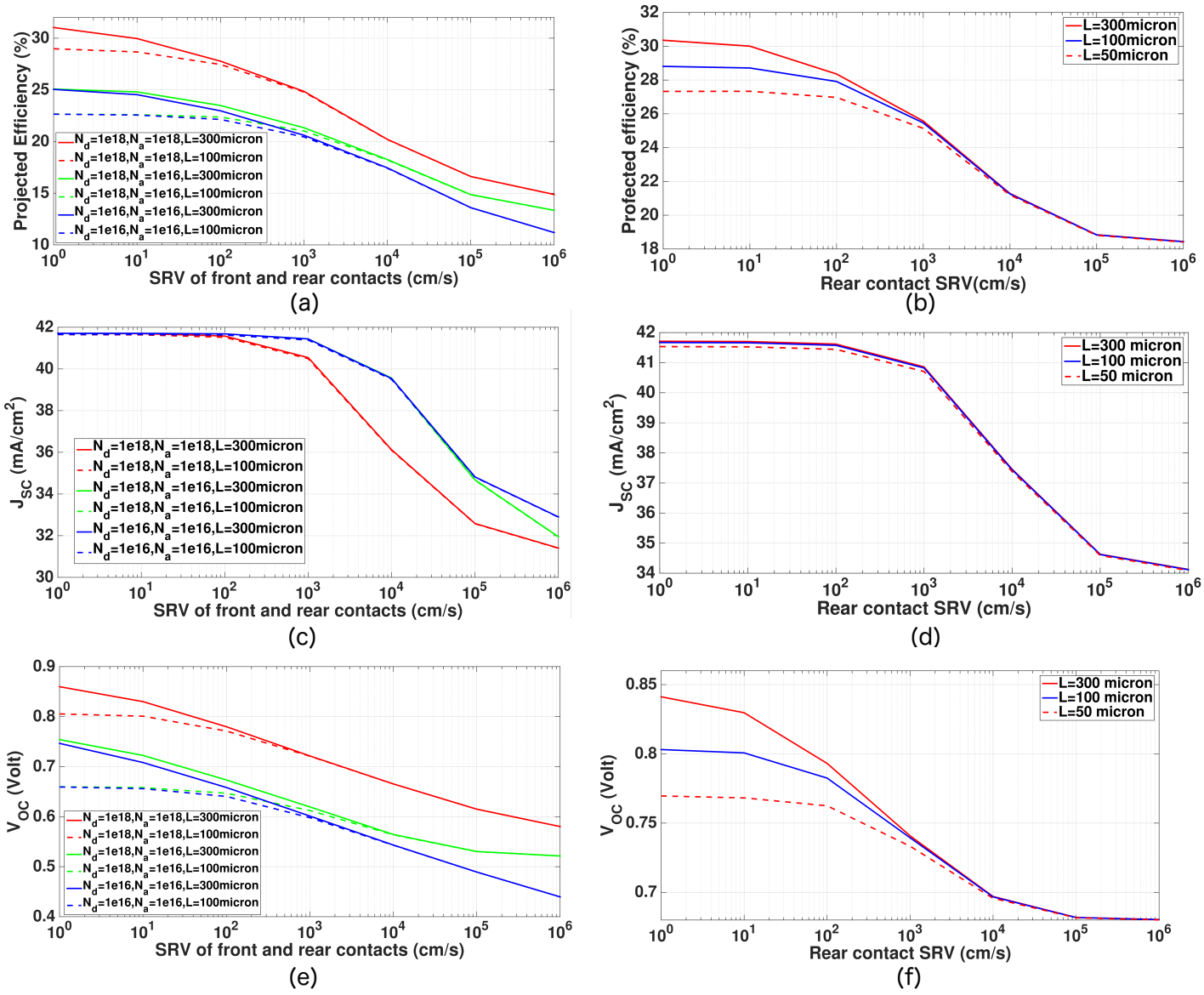

Figure 10. Effect of SRV_{front} and SRV_{rear} on solar cell performance. The plots on the left column corresponds to simultaneous variation of SRV_{front} and SRV_{rear} and those on the right column corresponds to varying only SRV_{rear} keeping SRV_{front} fixed at 10 cm/s. The diffusion length is assumed to be doping independent. For the plots in the right column we set $N_a = N_d = 10^{18}$ cm^{-3}. The plots show that over a SRV range of $1 - 10^3$ cm/s, V_{OC} drops off more strongly than J_{SC}.

length. On the other hand, high doping is advantageous for achieving high V_{OC}. The trade-off between doping concentration and diffusion length leads to an optimum doping. Figure 9(b) shows that η reaches its maximum value of 27.9% for $N_d = 2 \times 10^{18}$ cm^{-3} and $N_a = 2 \times 10^{17}$ cm^{-3} when the junction is 100 nm below the top surface of the cell. Note that this is well beyond the current record efficiency of 26.3% [1, 4].

Fig. 10 shows the effect of the front and rear SRVs on the performance of the solar cell under different doping levels. Here again, we treat diffusion length as a variable independent of doping to accommodate possible lifetimes of the order of milliseconds, potentially achieved by advanced material processing technologies such as hydrogenation of Si [44]. Figure 10(a), (c) and (e) correspond to the case when both SRV_{front} as well as SRV_{rear} are varied (maintaining

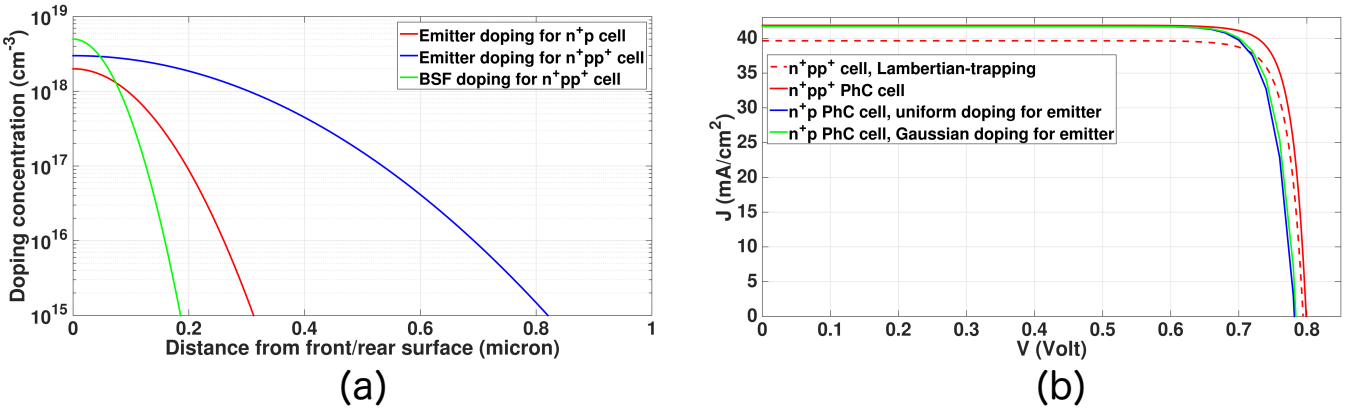

Figure 11. (a) Gaussian doping profile for n^+ emitter in n^+p type cell and n^+/p^+ regions in n^+pp^+ type cell. (b) Comparison of $J-V$ characteristics of n^+p cell with uniform emitter doping ($\eta = 27.82\%$), n^+p cell with Gaussian emitter doping ($\eta = 28.05\%$) and n^+pp^+ cell ($\eta = 29.11\%$) with Gaussian doping for ~ 170 nm thick n^+ and p^+ regions. For n^+p cell, the junction is situated 170 nm below the top passivation-Si interface. For n^+pp^+ cell, the p region is uniformly doped with $N_a = 5 \times 10^{15}$ cm^{-3}. n^+pp^+ cell exhibits $V_{OC} = 0.799$ V. Red dashed curve corresponds to the $J-V$ characteristic of n^+pp^+ cell that employs perfect-Lambertian light trapping ($J_{MAPD} = 39.65$ mA/cm^2). Without slanted parabolic-pore PhC-assisted light-trapping the n^+pp^+ cell would have $\eta = 27.26\%$. All the calculations take into account Richter's improved Auger model.

$SRV_{rear} = SRV_{front}$). Fig. 10(b), (d) and (f) correspond to varying SRV_{rear} alone keeping SRV_{front} fixed at 10 cm/s and doping levels for base and emitter fixed at 10^{18} cm^{-3}. Fig. 10(a), (c) and (e) show that diffusion length becomes a decisive factor for low SRVs. For SRVs beyond 1000 cm/s, there is no difference between $L = 300$ μm and $L = 100$ μm. However, at $SRV_{front} = SRV_{rear} = 10$ cm/s changing the diffusion length from 100 μm to 300 μm results in $\sim 2\%$ increase in the efficiency. Fig. 10(c), (d), (e) and (f) show that J_{SC} remains relatively insensitive to the variation of SRV below 10 cm/s and diffusion lengths longer than 50 μm. In contrast, for long diffusion lengths, V_{OC} falls off rapidly with SRV. Further, fig. 10(b) shows that with $N_a = N_d = 10^{18}$ cm^{-3} and $L = 50$ μm ($\tau_{neff} = 3.5$ μs and $\tau_{peff} = 6$ μs) we can achieve above 27% conversion efficiency for $SRV_{front} = SRV_{rear} = 10$ cm/s.

In general, moving the junction away from the top surface of the solar cell is detrimental to efficiency due to increased distance that low-mobility, minority holes must diffuse to escape the region of high Auger recombination. For example, if the position of the pn-junction is moved from 100 nm to 170 nm below the top passivation-Si interface while maintaining the optimum doping concentration, the projected efficiency of the cell drops to 27.82%. However, using a 170 nm Gaussian doping profile (Fig. 11a) for the emitter $J-V$ characteristics (fig. 11b) reveals a slightly improved FF leading to a 28.05% conversion efficiency. The Gaussian doping profile for the emitter is given by $N = N_{f0}\exp(-z^2/2\sigma_f^2)$ where, $N_{f0} = 2 \times 10^{18}$ cm^{-3}, $\sigma_f = 80$ nm and z denotes the distance from the passivation-silicon interface. The efficiency is further improved using Gaussian doping profiles (~ 170 nm thick) for both n^+ and p^+ regions with relatively low, uniform doping ($N_a = 5 \times 10^{15}$ cm^{-3}) throughout the interior. For the front n^+ region, we choose $N_{f0} = 3 \times 10^{18}$ cm^{-3} and $\sigma_f = 45$ nm, whereas for the rear p^+ region, we choose $N_{r0} = 5 \times 10^{18}$ cm^{-3} and $\sigma_r = 45$ nm (fig. 11a). Fig. 11b shows that the n^+pp^+ cell exhibits 29.11% power conversion efficiency due to significantly improved V_{OC} and FF. In order to highlight the improvement provided by PhC-assisted wave-interference based light-trapping, we show the $J-V$ characteristic of the same 10 μm-thick n^+pp^+ cell assuming

Cell type	Thickness(μm)	J_{SC} (mA/cm^2)	V_{OC} (V)	$FF(\%)$	$\eta(\%)$
Photonic crystal n^+p cell, junction at 100 nm, uniformly doped emitter	10	41.70	0.7836	85.49	27.94
Photonic crystal n^+p cell, junction at 170 nm, uniformly doped emitter	10	41.70	0.7817	85.35	27.82
Photonic crystal n^+p cell, junction at 170 nm, emitter with Gaussian doping profile	10	41.70	0.7839	85.80	28.05
Photonic crystal n^+pp^+ cell, 170 nm thick n^+ and p^+ regions with Gaussian doping profile	10	41.72	0.7990	87.32	29.11
Kaneka Corporation	165	42.3	0.7440	83.80	26.30
PERL	400	42.7	0.7060	82.80	24.96

Table I. Comparison of proposed PhC thin-silicon solar cells using the Auger recombination model with existing high-efficiency single-junction solar cells. For the n^+p and n^+pp^+ PhC solar cells, the $p-$type substrate is uniformly doped with $N_a = 2 \times 10^{17}$ cm^{-3} and 5×10^{15} cm^{-3}, respectively.

perfect Lambertian light-trapping with MAPD of 39.65 mA/cm^2. The hypothetical Lambertian n^+pp^+ cell provides only 27.26% conversion efficiency with $J_{SC} = 39.65$ mA/cm^2, $V_{OC} = 0.7945$ V, $FF = 86.55\%$. Our slanted parabolic-pore PhC cell offers nearly 2% more (additive) power conversion efficiency than the hypothetical cell constrained by the Lambertian limit.

Table I compares our proposed high-efficiency thin-silicon solar cells with the 25% efficient PERL cell and the record efficiency holding $c-Si$ solar cell recently fabricated by Kaneka Corporation [5]. This comparison suggests our PhC solar cells may outperform the thicker cells by achieving a higher V_{OC} through reduced bulk recombination. The transport results for our PhC cells in tab. I have been cross-checked using TCAD Sentaurus [49] and Richter's improved Auger model [45].

V. PRACTICAL CONSIDERATIONS

In this section, we consider several real-world issues that could decrease the projected efficiency of our cell from over 29%. These include the use of lossy metals instead of PEC for the rear contact and back-reflector, power loss in the emitter region due to sheet resistance and increased surface recombination velocity. We do not explicitly consider shadowing loss of the front contacts given recent advances in broad-band, wide-angle cloaked-contacts [34–37] and interdigitated back contacts (IBC) [5, 30–32].

Silver is a useful contact material due to its very low resistivity. As a back-reflector Ag sometimes yields non-ideal reflectivity ($\sim$ 96%) [52] and the associated parasitic absorption can reduce MAPD by $0.3 - 0.8$ mA/cm^2 [12, 18, 51, 53]. In contrast, we consider a combination of SiO_2 and Ag which has above 99% reflectivity [52]. Our SiO_2-PEC mimics the near-perfect reflectivity of a $SiO_2 - Ag$ back-reflector. To demonstrate this, we implement the wavelength dependent n and k (real and imaginary parts of refractive index) of Ag through accurate fitting of

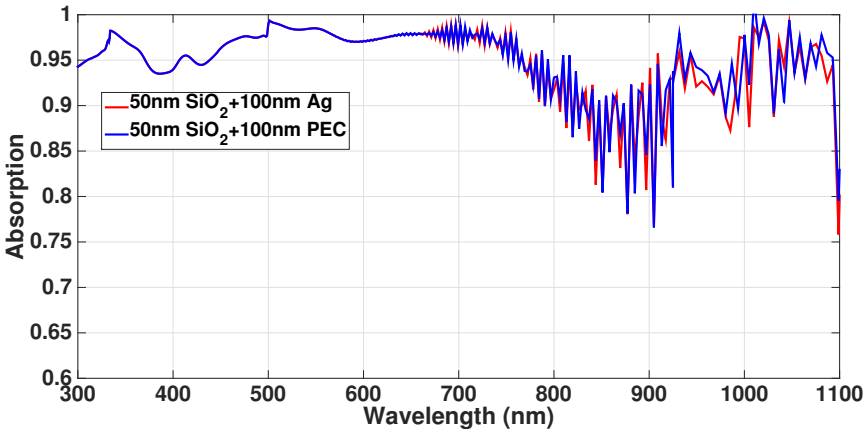

Figure 12. Comparison of absorption spectra of optimized slanted parabolic-pore PhC with Ag and PEC back-reflectors. Ag back-reflector causes 0.04 mA/cm^2 drop in MAPD in comparison to PEC back-reflector. Thus, the efficiency of the solar cell remains practically unaffected by use of Ag back-reflector. This result is consistent with simulations carried out in [52], where it has been shown that SiO_2-Ag combination has more than 99% reflectivity in comparison to Ag alone ($\sim$ 96% reflectivity).

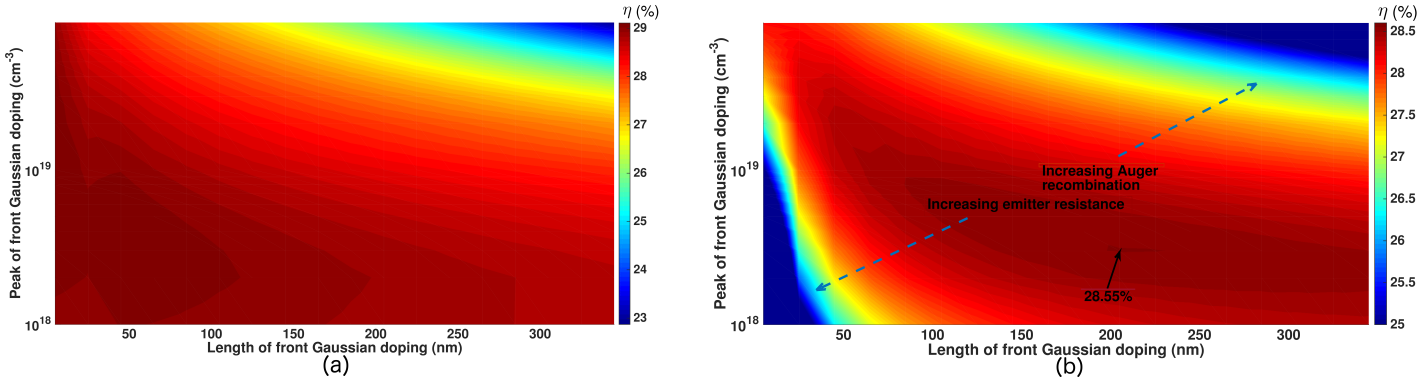

Figure 13. Emitter optimization of slanted parabolic-pore PhC solar cell: (a) neglecting power-loss in the emitter, (b) including power-loss in the emitter. The finger-spacing is assumed to be 800 μm (same as the 25% PERL cell [20]). Including sheet-resistance, a maximum efficiency of 28.55% is obtained for $N_{f0} = 3 \times 10^{18}$ cm^{-3} and $\sigma_f = 205$ nm. This is equivalent to an emitter width of 730 nm and sheet-resistance of 362 Ω/sq.

experimental data [54] with the Drude critical point model [55]. Figure 12 compares the absorption spectra of the optimized slanted parabolic-pore PhC with $SiO_2 - Ag$ and SiO_2- PEC back-reflectors in absence of ARC. These absorption spectra correspond to 41.56 and 41.6 mA/cm^2 MAPDs, respectively.

We now consider the issue of sheet-resistance in emitter-design optimization. Figure 13(a) shows the emitter optimization map with respect to the peak donor concentration N_{f0} and emitter Gaussian-width, neglecting sheet-resistance. For a given σ_f, as N_{f0} increases the emitter field-gradient increases, improving the collection of majority electrons while repelling the minority holes. However, a greater N_{f0} increases Auger recombination. For a given σ_f, N_{f0} exhibits an optimum balance between the Auger recombination and front surface field. As σ_f decreases, bulk recombination in the cell decreases. Near our bottom contact, we use a 170 nm thick p^+ BSF with Gaussian doping profile and peak acceptor concentration $N_{r0} = 5 \times 10^{18}$ cm^{-3}. In fig. 13(a), we find, for the top contact, optimum

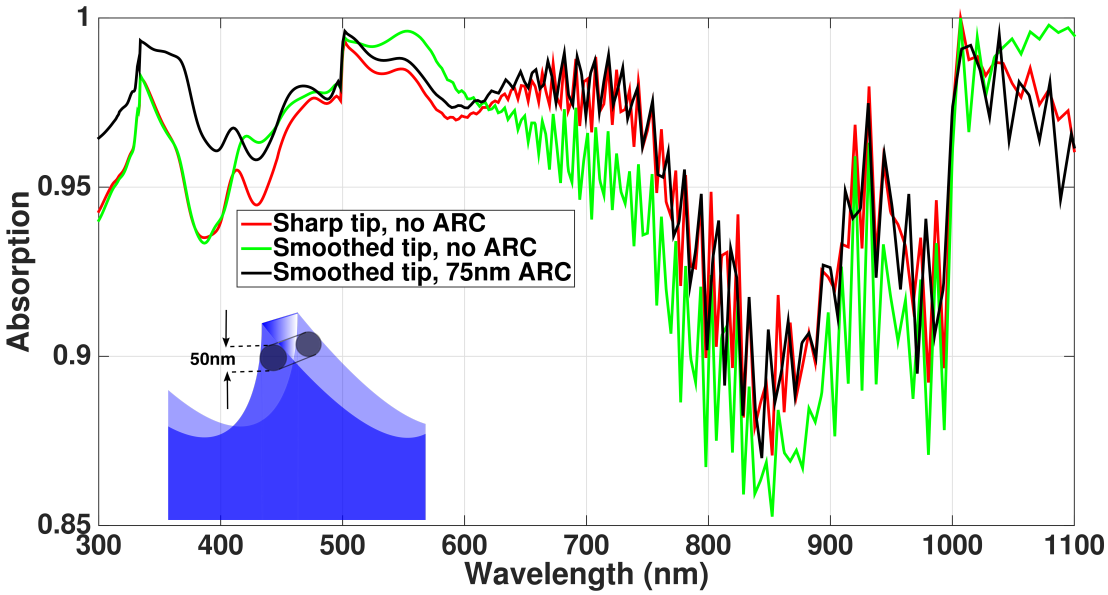

Figure 14. Absorption spectra of optimized slanted parabolic-pore PhC. Red curve: unperturbed (i.e. with sharp tip) slanted parabolic-pore PhC (without ARC), corresponding to $J_{MAPD} = 41.6$ mA/cm^2; green curve: PhC with smoothed tip (without ARC), corresponding to $J_{MAPD} = 41.3$ mA/cm^2; black curve: PhC with smoothed tip and 75 nm ARC, corresponding to $J_{MAPD} = 41.71$ mA/cm^2. The inset shows the model used to simulate smoothed tip.

values of $N_{f0} = 3 \times 10^{18}$ cm^{-3} and $\sigma_f = 45$ nm for a conversion efficiency of 29.1%. This corresponds precisely to our choice of 170 nm overall emitter-width for our $1D$ model of the n^+pp^+ cell.

In practice, emitter-thickness must be large enough to prevent ion migration from front contact to the shallow junction. Also, with decreasing emitter-width, the lateral component of the emitter-current has to flow to the nearest contact finger through a narrower region. The resulting sheet-resistance is a further source of power-loss. The power-loss (P_{loss}) in the emitter due to sheet resistance can be estimated as a fraction of the generated power P_{gen} [56]. The actual efficiency of a real-world solar cell is: $\eta_{actual} = \eta\,(1 - {}^{P_{loss}}/_{P_{gen}})$. For concreteness, we consider a cell with finger-spacing of 800 μm and finger-width of 20 μm as deployed in the 25% efficient PERL cell [20] and a more recent Tunnel Oxide Passivated Contact (TOPCon) cell [57]. Feldmann et al. [57] have shown that for 800 μm finger-spacing and 20 μm low-resistivity Ag finger-width, resistance-loss in the finger is negligible. The sheet-resistances corresponding to different N_{f0} and σ_f are calculated using PV Lighthouse sheet-resistance calculator [58]. The emitter optimization map including sheet-resistance, is shown in fig. 13(b). As the emitter-width decreases, the sheet-resistance increases while Auger recombination decreases, leading to a revised optimum emitter doping profile. A maximum efficiency of 28.55% is achieved for $N_{f0} = 3 \times 10^{18}$ cm^{-3} and $\sigma_f = 205$ nm (equivalently, an emitter-width of 730 nm). The sheet-resistance at this optimum point is 362 Ω/sq. In this concrete example of upper contact geometry with emitter sheet resistance included, the projected efficiency drops only slightly from its previously estimated value of 29.11%.

Another source of unwanted recombination at the front surface of our cell is the sharp tip between two parabolic pores. These sharp protrusions can be smoothed during the fabrication process with negligible loss in light-trapping

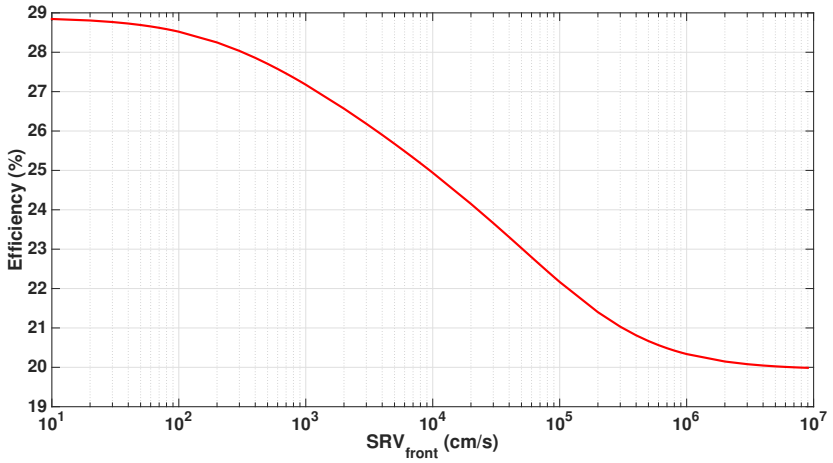

Figure 15. Dependence of efficiency of optimized slanted parabolic-pore PhC solar cell on SRV_{front}. SRV_{rear} is kept fixed at 20 cm/s.

and solar absorption. We model this smoothing by replacing the knife-edge with a 50 nm diameter cylinder. Figure 14 shows that this rounded tip causes more reflection in the $625-1000$ nm spectral range, reducing the MAPD to 41.3 mA/cm^2. However, the addition of a 75 nm non-conformal ARC on the rounded tips brings the MAPD up to 41.71 mA/cm^2, just shy of the previously quoted optimum of 41.72 mA/cm^2. This shows that our PhC structure is robust to small variations in fabrication that at the same time remove unwanted recombination centers.

Finally, we consider the effect of increased front contact SRV on the performance of our proposed cell. Experimental studies by Min et al. have shown that front SRV (SRV_{front}) of SiN_x-passivated $c-Si$ solar cells with industrial emitters may exceed 10^3 cm/s [27]. On the other hand Kerr et al. have shown that emitters passivated with annealed thin-oxide (SiO_2) has lower $SRV_{front} \sim 200$ cm/s [59]. Also, the effective SRV_{rear} for PERC cells are $\sim 15-20$ cm/s [25, 60]. Figure 15 shows the variation of efficiency with SRV_{front} for fixed $SRV_{rear} = 20$ cm/s. At $SRV_{front} = 200$ cm/s, the conversion efficiency of our cell is 28.25% ($\sim 0.6\%$ less than efficiency at $SRV_{front} = 10$ cm/s). Overall, these real-world considerations yield a projected efficiency close to 28% when proper optimization is done.

VI. CONCLUSIONS

In summary we have shown that using wave-interference-based light-trapping it is possible to absorb sunlight in the wavelength range of $300-1100$ nm, in a 10 μm-thick crystalline silicon solar cell, corresponding to a photocurrent density of 41.7 mA/cm^2 out of a maximum available 43.5 mA/cm^2. In this parabolic-pore photonic crystal with a lattice constant of 1000 nm, we identified the important role of $x-y$ symmetry breaking in absorbing near-infrared light through parallel-to-interface refraction into slow-light modes. The resulting solar absorption exceeds the Lambertian limit of 39.65 mA/cm^2.

It is likely that bandgap narrowing effects in crystalline silicon [61] would enable absorption of sunlight throughout the range of $300 - 1165$ nm. In this case the total available sunlight corresponds to a MAPD of 45.12 mA/cm^2. In this case, our optimized slanted-pore structure would reach a MAPD of 43.3 mA/cm^2 instead of 41.7 mA/cm^2 found for the narrower spectral window. This might more than offset the slight decrease in V_{OC} and possibly lead to higher power conversion efficiency than our present estimates.

Our electronics model consisted of a simple doping profile with $100 - 170$ nm $n-$type silicon at top with a donor concentration of 2×10^{18} cm^{-3} and a large $p-$type silicon region below with acceptor concentration of 2×10^{17} cm^{-3}. Using an Auger recombination model for the bulk, we found a power conversion efficiency of about 28% when the effective surface recombination velocities at the top and bottom were reduced to 10 cm/s. In this Auger model for bulk carrier recombination, the carrier diffusion length is fixed by the doping concentration. The combination of wave-interference-based light-trapping in thin-silicon and low surface recombination velocities offer route to efficiencies above 29% within the Auger recombination model. This has been achieved using a more elaborate doping profile. For instance, bulk Auger recombination can be greatly reduced by lowering the doping concentration to 5×10^{15} cm^{-3} throughout the most of the acceptor $p-$region, but increasing the donor and acceptor doping to above 10^{18} cm^{-3} according to a Gaussian profile in a narrow 170 nm region near the top and bottom contacts. Such a profile allows the solar cell to maintain a high V_{OC} while at the same time reducing bulk recombination losses.

Finally, real-world effects, such as sheet-resistance and increased recombination velocity near the top contact still yield a projected power conversion efficiency of about 28%. Consideration of sheet-resistance allows us to identify optimum emitter design with Gaussian doping. A maximum conversion efficiency of 28.55% is achieved for a peak emitter doping of 3×10^{18} cm^{-3} and 730 nm emitter-thickness. This configuration provides the best balance between recombination-loss in the emitter and power-loss due to sheet-resistance for a specific choice of upper contact spacing. Overall, the parabolic-pore PhC with PERC architecture offers unprecedented power conversion efficiency with only 10 μm $c - Si$. Other architectures worthy of study are single heterojunction-IBC (SHJ-IBC) and TOPCon cells. TOPCon cells considered by Feldmann et al. [57] offer higher efficiency owing to improved V_{OC} compared to conventional PERT cell. Also, single heterojunction cells offer higher V_{OC} due to the wider band gap of amorphous Si.

Our theoretical roadmap for light-trapping nanostructure design, doping profiles and surface passivation offers a number of routes to thin-silicon solar cells that surpass the power conversion efficiency of any single-junction silicon solar cell to date. It is hoped that these results will motivate experimental and fabrication efforts to realize the required structures.

ACKNOWLEDGEMENT

We are grateful to Prof. S. Y. Lin and Dr. P. Kuang for valuable discussions. This work was supported by the United States Department of Energy DOE-BES in a subcontract under award DE-FG02-06ER46347.

[1] Best Research-Cell Efficiencies (NREL, 2016), `https://www.nrel.gov/pv/assets/images/efficiency-chart.png`

[2] W. Shockley and H. J. Queisser, "Detailed balance limit of efficiency of p-n junction solar cells", J. of Appl. Phys. 32, 510 (1961).

[3] A. Richter, M. Hermle, and S. W. Glunz, "Reassessment of the limiting efficiency for crystalline silicon solar cells", IEEE J. of Photovoltaics 3, 1184 (2013).

[4] M. A. Green, K. Emery, Y. Hishikawa, W. Warta, E. D. Dunlop, D. H. Levi and A. W. Y. Ho-Baillie, Solar cell efficiency tables (version 49), Prog. Photovolt: Res. Appl. 25, 3–13 (2016).

[5] K. Yoshikawa, H. Kawasaki, W. Yoshida, T. Irie, K. Konishi, K. Nakano, T. Uto, D. Adachi, M. Kanematsu, H. Uzu and K. Yamamoto, "Silicon Heterojunction solar cell with interdigitated back contacts for a photoconversion efficiency over 26%", Nature Energy 2, 17032 (2017).

[6] S. Hargreaves, L. E. Black, D. Yan and A. Cuevas, "Modelling of silicon solar cells with up-to-date material parameters", Energy Procedia 38, 66-71 (2013).

[7] S. Y. Herasimenka, W. J. Dauksher and S. G. Bowden, "> 750 mV open circuit voltage measured on 50 μm thick silicon heterojunction solar cell", Applied Physics Letters 103, 053511 (2013).

[8] S. Yoshiba, M. Hirai, Y. Abe, M. Konagai and Y. Ichikawa, "Single crystalline silicon solar cells with rib structure", AIP Advances 7, 025104 (2017).

[9] S. John, "Strong localization of photons in certain disordered dielectric superlattices", Phys Rev. Lett 58, 2486 (1987).

[10] E. Yablonovitch, "Inhibited spontaneous emission in solid-state physics and electronics", Phys. Rev. Lett. 58, 2059 (1987).

[11] G. Demsey and S. John, "Solar energy trapping with modulated silicon nanowire photonic crystals", J. Appl. Phys. 112, 074326 (2012).

[12] S. Eyderman, S. John and A. Deinega, "Solar light trapping in slanted conical-pore photonic crystals: Beyond statistical ray trapping", J. Appl. Phys. 113, 154315 (2013).

[13] S. Eyderman, S. John, M. Hafez, S. S. Al-Ameer, T. S. Al-Harby, Y. Al-Hadeethi and D. M. Bouwes, "Light-trapping optimization in wet-etched silicon photonic crystal solar cells", J. Appl. Phys. 118, 023103 (2015).

[14] A. Chutinan and S. John, "Light trapping and absorption optimization in certain thin-film photonic crystal architectures", Phys. Rev. A 78, 023825 (2008).

[15] T. Tiedje, E. Yablonovitch, G. Cody, and B. Brooks, "Limiting efficiency of silicon solar cells," IEEE Trans. on Electron Devices 31, 711 (1984).

[16] A. Mavrokefalos, S. E. Han, S. Yerci, M. S. Branham and G. Chen, "Efficient Light Trapping in Inverted Nanopyramid Thin Crystalline Silicon Membranes for Solar Cell Applications", Nano Lett., 12, 2792–2796 (2012).

[17] M. S. Branham, W. Hsu, S. Yerci, J. Loomis, S. V. Boriskina, B. R. Hoard, S. E. Han and G. Chen, "15.7% Efficient 10-μm-Thick Crystalline Silicon Solar Cells Using Periodic Nanostructures", Adv. Mater. 27, 2182 – 2188 (2015).

[18] S. Foster and S. John, "Light-trapping design for thin-film silicon-perovskite tandem solar cells", J. Appl. Phys 120, 103103 (2016).

[19] P. Kuang, S. Eyderman, M. L. Hsieh, A. Post, S. John and S. Y. Lin, "Achieving an Accurate Surface Profile of a Photonic Crystal for Near-Unity Solar Absorption in a Super Thin-Film Architecture", ACS Nano 10, 6116 − 6124 (2016).

[20] A. Wang, J. Zhao and M. A. Green, "24% efficient silicon solar cells", Appl. Phys. Lett. 57, 602 − 604 (1990).

[21] M. A. Green, K. Emery, Y. Hishikawa and W. Warta, "Solar cell efficiency tables (version 37)", Prog. Photovolt: Res. Appl. 19, 84–92 (2011).

[22] A. Luque and A. Marti, "Increasing the Efficiency of Ideal Solar Cells by Photon Induced Transitions at Intermediate Levels", Phys. Rev. Lett. 78, 5014 − 5017 (1997).

[23] R. W. Peng, M. Mazzer, and K. W. J. Barnham, "Efficiency enhancement of ideal photovoltaic solar cells by photonic excitations in multi-intermediate band structures", Appl. Phys . Lett. 83, 770 − 772 (2003).

[24] K. Q. Le and S. John, "Synergistic plasmonic and photonic crystal light- trapping: Architectures for optical upconversion in thin-film solar cells", Opt. Express 22, $A1 - A12$ (2014).

[25] S. J. Robinson, S. R. Wenham, P. P. Altermatt, A. G. Aberle, G. Heiser and M. A. Green, "Recombination rate saturation mechanisms at oxidized surfaces of high- efficiency silicon solar cells", J. Appl. Phys. 78, 4740 − 4754 (1995).

[26] P. Mahtani, K. R. Leong, B. Jovet, D. Yeghikyan and N. P. Kherani, "High quality amorphous–crystalline silicon heterostructure prepared by grid-biased remote radio-frequency plasma enhanced chemical vapor deposition", J. of Non-Crystalline Solids 358, 3396 − 3402 (2012).

[27] B. Min, H. Wagner, A. Dastgheib-Shirazi, A. Kimmerle, H. Kurz, and P. P. Altermatt, "Heavily doped Si: P emitters of crystalline Si solar cells: recombination due to phosphorus precipitation", Phys. Status Solidi RRL 8, 680 − 684 (2014).

[28] R. S. Bonilla, B. Hoex, P. Hamer, and P. R. Wilshaw, "Dielectric surface passivation for silicon solar cells: A review", Phys. Status Solidi A 214, 1700293 (2017).

[29] A. W. Blakers, "Shading losses of solar-cell metal grids", J. of Appl. Phys. 71, 5237 (1992).

[30] E. V. Kerschaver and G. Beaucarne, "Back-contact solar cells: A review", Prog. Photovolt: Res. Appl. 14, 107 − 123 (2005).

[31] C. Battaglia, A. Cuevas, and S. D. Wolf, "High-efficiency crystalline silicon solar cells: status and perspectives", Energy Environ. Sci. 9, 1552 − 1576 (2016).

[32] M. K. Mat Desa, S. Sapeai, A. W. Azhari, K. Sopian, M. Y. Sulaiman, N. Amin, and S. H. Zaidi, "Silicon back contact solar cell configuration: A pathway towards higher efficiency", Renewable and Sustainable Energy Rev. 60, 1516–1532 (2016).

[33] S. Bhattacharya and S. John, to be published.

[34] M. F. Schumann, S. Wiesendanger, J. C. Goldschmidt, B. Blasi, K. Bittkau, U. W. Paetzold, A. Sprafke, R. B. Wehrspohn, C. Rockstuhl, and M. Wegner, "Cloaked contact grids on solar cells by coordinate transformations: designs and prototypes", Optica 2, 850 − 853 (2015).

[35] M. Langenhorst, M. F. Schumann, R. Schmager, J. Lehr, U. Lemmer, M. Wegener, B. Richards, and U. W. Paetzold, "Performance of Silicon Solar Cells with Cloaked Contact Fingers under Realistic Conditions", Light, Energy and the Environment, OSA Technical Digest (online), $PW2A.3$ (2017).

[36] M. F. Schumann, M. Langenhorst, M. Smeets, K. Ding, U. W. Paetzold, and M. Wegener, "All-Angle Invisibility Cloaking of Contact Fingers on Solar Cells by Refractive Free-Form Surfaces," Adv. Opt. Mater. 1700164 (2017).

[37] E. S. Roman, A. Vitrey, J. Buencuerpo, I. Prieto, J. M. Llorens, A. Garcia-Martin, B. Alen, A. Chaudhuri, A. Neumann, S. R. J. Brueck, and J. M. Ripalda, "Cloaking of solar cell contacts at the onset of Rayleigh scattering", Sci. Rep., 28669 (2016).

[38] Z. R. Chowdhury, K. Cho and N. P. Kherani, "High-quality surface passivation of silicon using native oxide and silicon nitride layers", Appl. Phys. Lett. 101, 021601 (2012).

[39] S. Calnan, O. Gabriel, I. Rothert, M. Werth, S. Ring, B. Stannowski and R. Schlatmann, "Influence of Chemical Composition and Structure in Silicon Dielectric Materials on Passivation of Thin Crystalline Silicon on Glass", ACS Appl. Mater. Interfaces 7, 19282–19294 (2015).

[40] I. Valuev, A. Deinega, A. Knizhnik and B. Potapkin, "Creating Numerically Efficient FDTD Simulations Using Generic C++ Programming", Lecture Notes in Computer Science 4707, 213 (2007).

[41] A. Deinega and S. John, "Finite difference discretization of semiconductor drift-diffusion equations for nanowire solar cells", Comp. Phys. Comm. 183, 2128 (2012).

[42] M. A. Green, "Self-consistent optical parameters of intrinsic silicon at 300 K including temperature coefficients", Solar Energy Materials and Solar Cells 92, 1305–1310 (2008).

[43] G. Masetti, M. Severi and S. Solmi, "Modeling of Carrier Mobility Against Carrier Concentration in Arsenic-, Phosphorus-, and Boron-Doped Silicon", IEEE Trans. on Electron Devices, Vol. ED-30, 764 (1983).

[44] B. J. Hallam, P. G. Hamer, S. R. Wenham, M. D. Abbott, A. Sugianto, A. M. Wenham, C. E. Chan, G. Q. Xu, J. Kraiem, J. Degoulange and R. Einhaus, "Advanced Bulk Defect Passivation for Silicon Solar Cells", IEEE Journal of Photovoltaics 4,88 − 95 (2014).

[45] A. Richter, S. W. Glunz, F. Werner, J. Schmidt and A. Cuevas, "Improved quantitative description of Auger recombination in crystalline silicon", Phys. Rev. B 86, 165202 (2012).

[46] T. Luder, G. Hahn and B. Terheiden, "Passivation of Si Wafers by ALD-Al_2O_3 Films with Different Surface Conditioning", Energy Procedia 8, 660 − 665 (2011).

[47] J. Benick, A. Richter, M. Hermle and S. W. Glunz, "Thermal stability of the Al_2O_3 passivation on p-type silicon surfaces for solar cell applications", Phys. Status Solidi RRL 3, 233 (2009).

[48] M. J. Kerr and A. Cuevas, "General parameterization of Auger recombination in crystalline silicon", J. Appl. Phys. 91, 2473 (2002).

[49] Synopsys, Synopsys TCAD, release $M - 2016.12$ (2016).

[50] A. Luque and I. Tobias, "Perimeter recombination in planar solar cells", J. of Appl. Phys. 73, 4042 (1993).

[51] S. Eyderman, A. Deinega, and S. John, "Near perfect solar absorption in ultra-thin-film GaAs photonic crystals," J. Mater. Chem. A 2, 761–769 (2014).

[52] H. Cui, P. R. Campbell, and M. A. Green, "Optimisation of the Back Surface Reflector for Textured Polycrystalline Si Thin Film Solar Cells", Energy Procedia 33, 118–128 (2013).

[53] Z. C. Holman, M. Filipic, B. Lipovsek, S. De Wolf, F. Smole, M. Topic, and C. Ballif, "Parasitic absorption in the rear reflector of a silicon solar cell: Simulation and measurement of the sub-bandgap reflectance for common dielectric/metal reflectors," Sol. Energy Mater. Sol. Cells 120, 426–430 (2014).

[54] P.B. Johnson and R.W. Christy, "Optical constants of the noble metals", Phys. Rev. B 6, 4370–4379 (1972).

[55] A. Vial, T. Laroche, M. Dridi, and L. L. Cunff, "A new model of dispersion for metals leading to a more accurate modeling of plasmonic structures using the FDTD method", Appl. Phys. A 103, 849 (2011).

[56] http://www.pveducation.org/pvcdrom/design/emitter-resistance

[57] F. Feldmann, M. Bivour, C. Reichel, M. Hermle, and S. W. Glunz, "Passivated rear contacts for high-efficiency $n-$type Si solar cells providing high interface passivation quality and excellent transport characteristics", Solar Energy Materials and Solar Cells 120, 270 (2014).

[58] PV Lighthouse sheet-resistance calculator, https://www2.pvlighthouse.com.au/calculators/Sheet%20resistance%20calculator/Sheet%20resistance%20calculator.aspx.

[59] M. J. Kerr, J. Schmidt, A. Cuevas, and J. H. Bultman, "Surface recombination velocity of phosphorus-diffused silicon solar cell emitters passivated with plasma enhanced chemical vapor deposited silicon nitride and thermal silicon oxide", J. Appl. Phys. 89, 3821 − 3826 (2001).

[60] M. Muller et al., "Loss analysis of 22% efficient industrial PERC solar cells", Energy Procedia 124, 131 − 137 (2017).

[61] A. Schenk, "Finite-temperature full random-phase approximation model of band gap narrowing for silicon device simulation", J. Appl. Phys. 84, 3684 − 3695 (1998).